Supplement of Earth Surf. Dynam., 5, 211–237, 2017
http://www.earth-surf-dynam.net/5/211/2017/
doi:10.5194/esurf-5-211-2017-supplement

Earth Surface Dynamics
Open Access
EGU

Supplement of

Validation of digital elevation models (DEMs) and comparison of geomorphic metrics on the southern Central Andean Plateau

Benjamin Purinton and Bodo Bookhagen

Correspondence to: Benjamin Purinton (purinton@uni-potsdam.de)

Each section in the Supplement is referenced to the section of interest in the main text (e.g., main text Sect. 3.1 is supplement Sect. S3.1.).

S3. Data and Methods

S3.1. dGPS Data

The collection of high-accuracy dGPS measurements over a large area on the Puna and its margins was conducted during field campaigns from March 2014-2016. Point measurements were collected with two Trimble ProXRS Pathfinder receivers, which logged measurements at 2-5 second intervals in roving modes. Most measurements were made with the unit attached to the roof of the field vehicle while traveling the unpaved roads on the high plateau and its margins. Additional measurements were conducted by fixing the units to backpacks to measure off-road features such as baselevel salar elevations, shorelines, fluvial-lacustrine terraces, and hillslope profiles. The Trimble ProXRS Pathfinder units used in the field rely on GPS L1 and P signals, allowing for centi- to decimeter accuracy in vertical and decimeter accuracy in horizontal measurements. In order to improve measurements to centimeter scale vertical accuracy, daily dGPS files were converted to RINEX format in Trimble Pathfinder Office™ and corrected with RTKLIB open source software for GNSS positioning (http://www.rtklib.com). Real-time kinematic post processing (RTKPOST) of all points was achieved using daily positional data from the International GNSS Service UNSA permanent station in Salta, Argentina (Fig. 1A) (ftp://data-out.unavco.org/pub/rinex/obs). For 333,555 measurements, minimum baseline distance to the UNSA permanent station was 8 km, maximum was 295 km, and the average was 157 km. Additional corrections were applied using global navigation broadcast files, satellite ephemerals, and rapid orbits acquired through NOAA (ftp://www.ngs.noaa.gov/cors/rinex). Positional files output by these tropo- and ionospheric corrections were referenced to the EGM96 / WGS84 datums and converted to merged shapefiles using the GDAL package for geospatial data management in a Python scripting environment (http://www.gdal.org/). Of the 333,555 total raw measurements from 2014-2016, 307,509 points with vertical and horizontal accuracies below 0.5 m were selected for the final dataset. Within this subset, 87.7 % of points have vertical accuracies below 0.2 m and 99.7 % of points had horizontal accuracies below 0.2 m (Fig. S1). The corrected dGPS shapefile contains irregularly spaced information determined by the speed at which the roving Trimble unit was moving, and were thus rasterized to the DEM of interest using the “Point to Raster” tool in ArcGIS, taking the average of all measurements within a pixel.

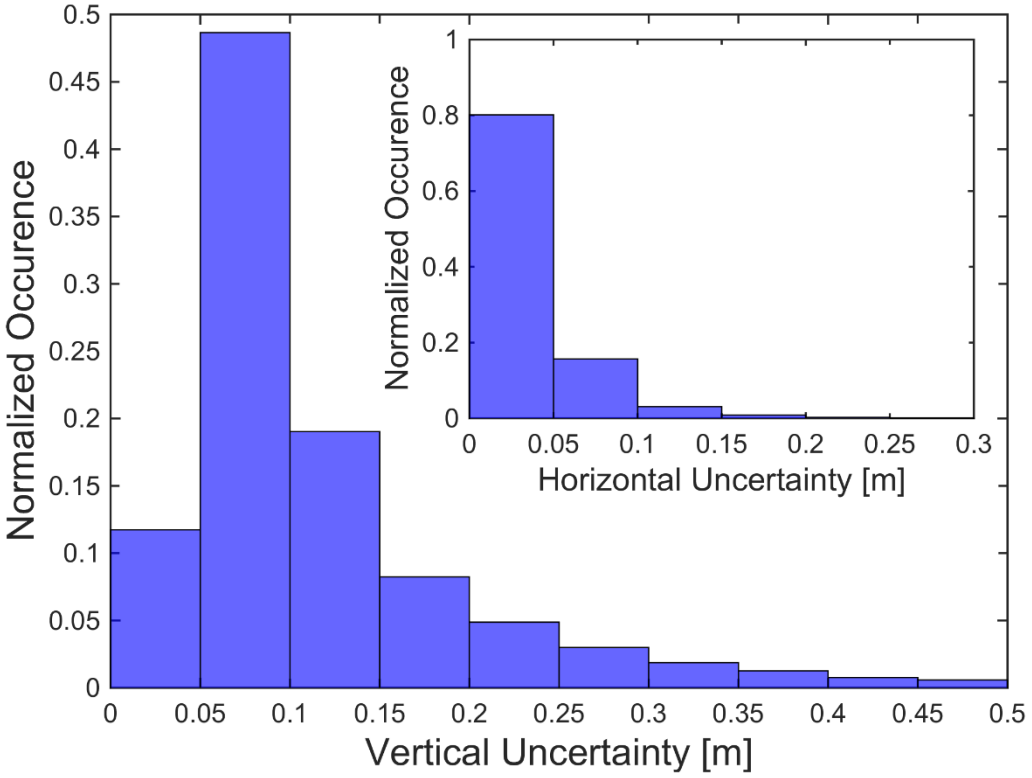

Figure S1. Normalized occurrence of vertical and horizontal (inset) uncertainties of 307,509 dGPS points with uncertainty below 0.5 m selected for DEM accuracy assessments. Correction of original 333,555 raw measurements was achieved using UNSA permanent station in Salta, Argentina. For location of Salta relative to measurements refer to Fig. 1A. 87.7 % of points have vertical accuracies below 0.2 m and 99.7 % of points have horizontal accuracies below 0.2 m.

S3.2. DEM Datasets

Here we provide details on the DEMs presented in Table 1 and used in the main manuscript (SRTM-C 30 m, ASTER GDEM2 30 m, ASTER L1A Stereopair Stack 30 m, ALOS World 3D 5 m and 30 m, TanDEM-X 12 m and 30 m, and single-CoSSC TerraSAR-X / TanDEM-X 10 m) along with a number of additional datasets that were not selected for full analysis (SRTMv4.1 90 m, SRTM-X 30 m, RapidEye 12 m, SPOT6 5 m, ALOS PRISM tri-stereopair 10 m, TerraSAR-X pairs 10 m, and single-CoSSC TerraSAR-X / TanDEM-X processed to 5 m).

SRTM

The SRTM flown aboard the Endeavour Shuttle in February 2000 collected Interferometric Synthetic Aperture Radar (InSAR) at wavelengths of 5.6 cm (C-band) and 3.1 cm (X-band) from 60º N to 56º S. Phase differences between sent and returned signals were used to extract elevation information and generate DEMs for 80 % of the globe free of charge to the scientific

community (Farr et al., 2007). C-band returns were used to generate DEMs at resolutions of 1 and 3 arc-seconds (30 and 90 m at the equator, respectively). The 30 m SRTM-C used in the present study was originally developed solely for the United States and only released for other areas in September 2014. Although some data voids persist in the SRTM-C 30 m, it is widely considered the highest quality global DEM publicly available, and thus chosen as the control for co-registration and selection of ground control points for optical DEM generation.

Despite the high quality of the SRTM-C data, root mean squared error (RMSE) can vary significantly above and below mission standard benchmarks (≤ 16 m; Rodriguez et al., 2006) and should be assessed on an individual basis to analyze terrain (slope and aspect) and land cover (vegetation and snow) effects (e.g., Sun et al., 2003; Berthier et al., 2006; Becek, 2008; Shortridge and Messina, 2011). Furthermore, reports have shown the actual realized resolution of the SRTM datasets is greater than the reported 1 and 3 arc-seconds, caused by final filtering steps to resample and remove noise (Smith and Sandwell, 2003; Tachikawa et al., 2011; Kolecka and Kozak, 2014).

First released in 2003, the hole-filled version of the 90 m SRTM C-band (SRTMv4.1) is available for public download at http://srtm.csi.cgiar.org/ (Jarvis et al., 2008). The SRTM mission standard vertical RMSE of ≤ 16 m and sub-pixel horizontal accuracy is often surpassed (Rodriguez et al., 2006), and because of this the 90 m SRTMv4.1 continues to be applied to geomorphic studies of regional hillslope and channel morphology (e.g., Forte et al., 2016). The SRTMv4.1 was originally considered in the present study for its global coverage and widespread use, and a complete dataset covering the study area was attained. The vertical uncertainty with respect to 64,515 rasterized dGPS measurements for the SRTMv4.1 was 2.59 ± 5.16 m (mean ± standard deviation) with a 0.44 % reduction after removal of ±30 m outliers. While this uncertainty was low, and within the range reported in other studies (e.g., Gorokhovich and Voustianiouk, 2006; Rexer and Hirt, 2014), we did not elect to apply further analysis on this 90 m data given the coarse resolution and availability of higher resolution 30 m global DEMs (SRTM-C, ASTER GDEM2, ALOS World 3D, and TanDEM-X).

Besides the DEMs generated by the SRTM C-band sensor, the SRTM X-band sensor was also used to generate a 1 arc-second (30 m) resolution DEM released in December 2010 by the German Aerospace Center DLR (DLR, 2010). Differences between the SRTM-C and SRTM-X band DEMs are caused by differences in swath coverage: The X-band sensor used single, or maximum double, coverage in cross section, whereas the C-band acquisitions were taken from multiple look directions and incidence angles. Therefore, the C-band achieved better coverage of layover and shadowed areas resulting in a smoother appearance compared with the SRTM-X (Marschalk et al., 2004). Poor quality of the SRTM-X DEM in high relief terrain is caused by terrain slope and aspect as well as the local incidence angle and radar beam geometry. On the other hand, errors in the SRTM-C DEM occur mostly in areas of original data voids that were later filled using interpolation or auxiliary data, and regions with steep slopes (e.g., Ludwig and Schneider, 2006; Kolecka and Kozak, 2014). Although the SRTM-X was noisier upon visual inspection and coverage over the present study area was sparse, we assessed dGPS vertical uncertainty over 20,682 rasterized dGPS measurements. Results indicate a vertical uncertainty of -5.48 ± 5.32 m with a 0.28 % ±30 m outlier reduction, which is within the range reported for other low vegetated regions (Ludwig and Schneider, 2006) and less than the uncertainty

found in vegetated regions (Kolecka and Kozak, 2014). Because of the lack of coverage over the Quebrada Honda and other parts of the study area, we did not use the SRTM-X for further assessment.

ASTER

Since its launch aboard NASA's Terra spacecraft in December 1999, the ASTER radiometer has collected along-track stereopairs with nadir (Band 3N) and backward (Band 3B) looking near infrared cameras between 83º N and 83º S (Tachikawa et al., 2011). With a base-to-height (B/H) ratio of 0.6 and an optical resolution of 15 m, the ASTER L1A 3N/B scenes are capable of providing stereogrammetric DEMs at spatial resolutions of 30 m with vertical RMSE between 7 and 15 m depending on scene quality and terrain relief (Toutin and Cheng, 2001; Hirano et al., 2003). Eight ASTER L1A stereopairs with variable overlap were collected from the Pocitos Basin for manual generation of 30 m DEMs in the ENVI™ software package. These DEMs were weighted based on their correlation with the SRTM-C and stacked to form a higher quality DEM (ASTER Stack). Ground control points (GCPs) for individual DEM generation were selected from the SRTM-C to provide an absolute vertical reference frame. Mean RMSE of GCPs was high at 7.53 pixels (113 m), likely caused by disagreements in geolocation between ASTER and SRTM (Kääb, 2005). On the other hand, mean tie point (TP) RMSE between identical points selected from the nadir and backward scenes during cross-correlation to extract height information was kept to 0.83 pixels (12 m). Table S1 lists all ASTER L1A scenes along with individual RMSE for the GCPs and TPs.

Table S1. ASTER L1A stereopairs and GCP and TP RMSE values from ENVI™.

ASTER scene full name	Date of capture	Number of GCPs	GCP RMSE (pixels)	Number of TPs	TP RMSE (pixels)
AST_L1A_00300000000000000_20140311171541_22799	September 9, 2009	11	1.66	70	1.14
AST_L1A_00309162000145723_20140311171541_22787	September 16, 2000	16	8.16	74	0.71
AST_L1A_00303302002144401_20160215104747_26594	March 30, 2002	9	8.80	115	0.94
AST_L1A_00304072005144209_20160216144251_7801	April 7, 2005	11	8.73	86	0.83
AST_L1A_00308192013144247_20160216144251_7791	August 19, 2013	11	8.58	84	0.85
AST_L1A_00309262015144253_20160216144251_7786	September 26, 2015	10	7.77	80	0.58
AST_L1A_00312092007144229_20160216144251_7796	December 9, 2007	11	8.51	81	0.69
AST_L1A_00312212000145514_20160216144251_7803	December 21, 2000	11	8.01	83	0.92

ALOS

Launched in 2006, the Advanced Land Observing Satellite (ALOS) Panchromatic Remote-sensing Instrument for Stereo Mapping (PRISM) provides another optical satellite source of DEMs (Tadono et al., 2014). With along-track nadir, backward, and forward viewing cameras at 2.5 m resolution providing a maximum B/H ratio of 1, the generation of DEMs at 5 m resolution with vertical and horizontal accuracy < 5 m RMSE is possible (Gonçalves, 2008; Trisakti and Julzarika, 2013). A PRISM tri-stereopair with partial coverage of the Pocitos Basin captured on April 26, 2010 was purchased and processed into a 10 m DEM in PCI-Geomatica™ (which allows bundle adjustment on the three scenes, a feature unavailable in ENVI™). GCP RMSE from the SRTM-C selection process was 0.6 pixels (1.5 m), and TP RMSE between the three scenes was 0.11 pixels (0.3 m). Final PRISM DEM resolution was set to 10 m to avoid persistent errors and artifacts from the 5 m output. Manual editing to remove large artifacts was carried out in the final step of DEM extraction. Additional smoothing in Matlab™ included high-frequency slope and curvature filtering, interpolation of small voids using the surrounding pixel neighborhood, filling of large voids with the SRTM-C resampled to 10 m, and Wiener (Wiener, 1949) adaptive filtering of the final DEM. Despite multiple attempts at DEM generation and post-processing, the noise remaining in the PRISM tri-stereopair DEM proved insurmountable to geomorphic application.

Similar to the ASTER GDEM endeavor, the ALOS team developed a global DEM (ALOS World 3D 5 m) from autocorrelation and stacking of approximately three million PRISM tri-stereopairs (Tadono et al., 2014; Takaku et al., 2014). Although this high-resolution DEM is only available through commercial purchase, in May 2016 the Japanese Aerospace Exploration Agency (JAXA) released a free 30 m version with terrestrial coverage from 82º N to 82º S (http://www.eorc.jaxa.jp/ALOS/en/aw3d30/). This dataset was downloaded for the entire area covered by the dGPS measurements. Although the 30 m ALOS World 3D contains numerous voids in the study area, coverage over the Quebrada Honda catchment was complete. In addition, a 580 km^2 clip of the original 5 m DEM covering the Quebrada Honda was purchased after failure to generate a sufficient DEM for geomorphic application from the raw PRISM tri-stereopair. Mission specifications of < 5 m horizontal and vertical RMSE for the World 3D, exceed the SRTM and ASTER mission standards (Tadono et al., 2014), but have yet to be thoroughly assessed.

PRISM tri-stereopair DEMs have been used in previous studies of glacier elevation change (e.g., Holzer et al., 2015) because of their low elevation uncertainty: 3.0 ± 4.52 m over 25,471 dGPS measurements and 0.37 % ±30 m outlier reduction in the present study. However, the mountainous terrain of the Pocitos Basin and its high relief made it difficult to generate a DEM of sufficiently low noise to allow slope and curvature calculation required by geomorphic applications. As in the case of stacking of ASTER L1A stereopair DEMs (ASTER Stack and ASTER GDEM2), the improvement after stacking and averaging of many ALOS PRISM tri-stereopairs is evident in the ALOS World 3D 5 and 30 m DEMs selected for the main manuscript. Therefore, stacking of several manually generated PRISM tri-stereopair DEMs would likely improve accuracy. We do note the tendency of optical DEMs to struggle in flat, low contrast topography (e.g., Berthier and Toutin, 2008), as in the case of the Salar de Pocitos in the present study.

TerraSAR-X / TanDEM-X

The German DLR TerraSAR-X mission launched in 2007 originally collected single pass radar pairs weeks to months apart at various baselines with non-ideal conditions for DEM generation (TerraSAR-X / TerraSAR-X pairs). This mission was bolstered in 2010 with the launch of the TanDEM-X satellite flown in tandem with TerraSAR-X to record radar pairs simultaneously and at an optimal baseline for DEM generation (Co-registered Single Look Slant Range Complex, or CoSSC, TerraSAR-X / TanDEM-X pairs). Interferometric unwrapping at the sub-wavelength scale of single-CoSSC TerraSAR-X / TanDEM-X pairs and stacking of several results was used to generate the 2016 released TanDEM-X 12 m DEM (and the edited commercial WorldDEM™ 12 m dataset available from AIRBUS Corp. since 2015). With a reported vertical accuracy of < 2 m RMSE in flat terrain (Krieger et al., 2013), we collected the 12 m TanDEM-X (and a down-sampled 30 m version) via research agreement DEM_CALVAL1028 with the DLR. Additionally, we generated local single-CoSSC TerraSAR-X / TanDEM-X DEMs for the Pocitos Basin at 10 m resolution through manual processing using techniques of interferometry (radar pairs also received under research agreement XTI_GEOL6727 with the DLR).

In addition to the standard 10 m CoSSC TerraSAR-X / TanDEM-X DEM generation procedure, we attempted to generate 5 m DEMs by using fewer azimuth and range looks but stacking several scenes. The study area is vegetation free and temporal decorrelation is minimal, but unfortunately we did not succeed in generating higher resolution DEMs from single-CoSSC TerraSAR-X / TanDEM-X radar pairs of sufficient quality for geomorphic applications. While vertical accuracy for these 5 m DEMs was generally low at < 5 m, visual inspection revealed many hillslope artifacts, which preclude accurate calculations of slope and curvature. We also generated several 10 m DEMs from TerraSAR-X / TerraSAR-X pairs using standard techniques, but because of large temporal differences between scenes, results continued to be of lower quality than the 10 m CoSSC TerraSAR-X / TanDEM-X DEMs, with vertical uncertainty > 10 m for many of the TerraSAR-X / TerraSAR-X DEMs. DEM stacking provided some improvement, but not enough for geomorphic application, given remaining hillslope artifacts. However, the improvement via stacking of many single-CoSSC TerraSAR-X / TanDEM-X DEMs at the DLR is evident in the high quality of the finished TanDEM-X DEM in our study.

RapidEye

We received an additional dataset of 10 RapidEye optical satellite scenes with a ground resolution of 6.5 m from the RapidEye Science Archive (Proposal ID 00195). Given the low incidence angles of the RapidEye scenes (maximum ~15º), we applied bundle adjustment on GCPs and TPs of six overlapping scenes in PCI-Geomatica™ (a feature not included in ENVI™), which provided a maximum B/H ratio of only ~0.2. After numerous attempts at reconfiguring GCPs (final mean RMSE of 3.71 m and 3.77 m in X and Y directions, respectively) and TPs (final mean RMSE of 3.19 m and 3.58 m in X and Y directions, respectively), combining different scenes, testing different output resolutions (12-20 m), and post-processing outputs using smoothing algorithms, we were unable to generate a DEM of sufficient quality for geomorphic application. Final dGPS uncertainty was high at -2.17 ± 12.28 m (n = 22,729), excluding the ±30 m outliers.

SPOT6

Two SPOT6 optical satellite scenes with a ground resolution of 1.5 m were also purchased commercially for the present study. The two scenes were collected at different times of the year (October 27, 2013 and April 13, 2014) with different shadowing, snow cover, and distortion. Although the scene incidence angles were sufficient for DEM generation (~5º and ~26º) we were unable to generate a high resolution (5 m) DEM of sufficient quality in ENVI™ or PCI-Geomatica™, because of moderate snow cover on the highest peaks, shadowing and distortion effects, and temporal distances between scenes. No dGPS uncertainty was calculated because SPOT6 DEM results were dominated by gross artifacts – 1,000+ meter steps or drops in elevation – and large no data voids.

S3.4. Geomorphic Applications

S3.4.1. Channel Profiles

The estimation of the *m/n* ratio [equivalent to θ, or concavity, in the equations of Hack (1957) and Flint (1974)] is necessary to normalize equation (1) across differently sized drainage areas for the mapping of regional patterns of deformation, climatic influence, and/or lithologic boundary conditions (e.g., Forte et al., 2016). As this *m/n* ratio falls in a restricted range (approximately 0.35-0.65), a reference value (typically 0.45) is often selected to calculate the normalized channel steepness index (k_{sn}) that can be compared across different-sized drainage areas (Wobus et al., 2006). However, in order to estimate a site-specific *m/n* from Eq. (1), power-law fitting of a linear regression on plots of log-binned area versus average slope is necessary. As slope-area regression requires careful consideration and the calculation of slope from noisy DEMs, Perron and Royden (2013) developed the method of chi plot channel profile analysis, which forgoes the need to calculate slope through integration of Eq. (1) and the introduction of a reference drainage area (A_0) to arrive at:

$$z(x) = z(x_b) + \left(\frac{U}{KA_0^m}\right)^{\frac{1}{n}}\chi \quad \text{(S1a)}$$

where

$$\chi = \int_{x_b}^{x}\left(\frac{A_0}{A(x)}\right)^{\frac{m}{n}} \quad \text{(S1b)}$$

In this equation z (elevation) is the dependent variable and χ (integral of drainage area along profile distance) is the independent variable, where x_b is the downstream baselevel start of integration. Using this transformation, channel profiles can be plotted linearly in chi space by estimating *m/n* using least-squares fitting and selection of the value with the highest R^2 correlation coefficient (Perron and Royden, 2013) or by fitting individual channel segments (Mudd et al., 2014).

The following details parameters used in the two chi plot techniques. The least-squares maximization method of Perron and Royden (2013) was implemented in TopoToolbox (https://github.com/csdms-contrib/topotoolbox) for Matlab™ (Schwanghart and Scherler, 2014) and the piece-wise fitting method of Mudd et al. (2014) was implemented in the LSDTopoTools (https://github.com/LSDtopotools) software package for Python. Only the trunk channel was selected for chi plot analysis as

the inclusion of tributaries led to very noisy results and a large range of *m/n* calculated depending on dataset and number of tributaries selected. Example plots from the 30 m SRTM-C for both methods are displayed in Figs. S2 and S3. For both techniques A_0 in Eq. (S1) was set to 1 km^2. All other parameters are specific only to the piece-wise fitting technique of Mudd et al. (2014).

For the piece-wise fitting, *m/n* values were tested from 0.35-0.75 with a step size of 0.01. Following parameter sensitivity tests, we calculated *m/n* with a minimum segment length of 14 nodes, a vertical uncertainty of 20 m (to account for elevation noise in the channel bed), a maximum 100 nodes tested at a time, and 250 Monte Carlo iterations for fitting. Only the mean node skip value was changed between the datasets from 2 to 5 to 10 for the 30, 10, and 5 m DEMs, respectively [see Mudd et al. (2014) for details of each parameter]. The *m/n* value was found to be most sensitive to vertical uncertainty as indicated by fluctuating values over the full range tested when changing the vertical uncertainty between runs. This is likely caused by over-fitting of the trunk channel with too many individual segments at lower uncertainty values (Mudd et al., 2014). We chose the blanket value of 20 m for vertical uncertainty given the narrow range of DEM resolutions (5-30 m). This value is greater than the SD from dGPS comparison (Table 2), but dGPS measurements occurred mostly in low-slope areas, and not in steep catchments where we expect higher uncertainties on valley bottoms from these satellite derived DEMs.

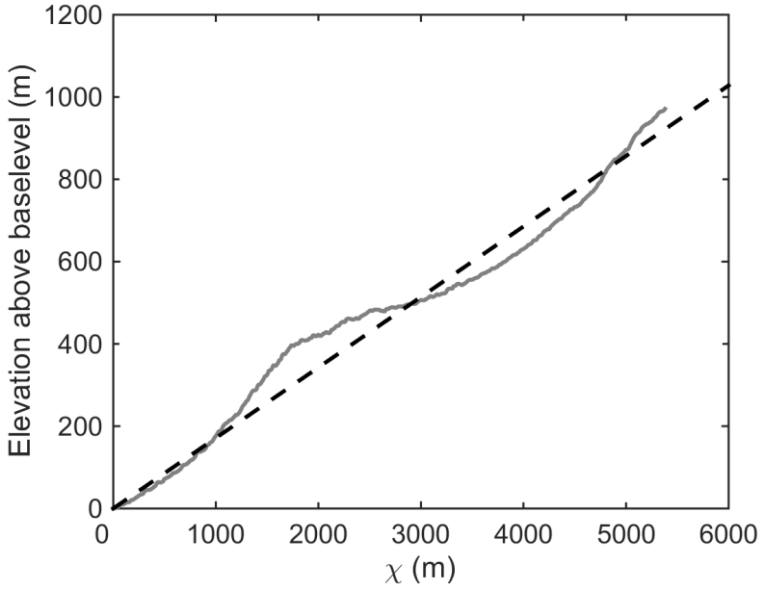

Figure S2. Chi plot analysis for the 30 m SRTM-C using least-squares maximization (Perron and Royden, 2013) implemented in Matlab (TopoToolbox; Schwanghart and Scherler, 2014). Channel is plotted as gray solid line with best-fit linear profile as black dashed line. Note the non-linearity of the channel caused by the knickpoint. Resulting *m/n* = 0.53 with R^2 = 0.97.

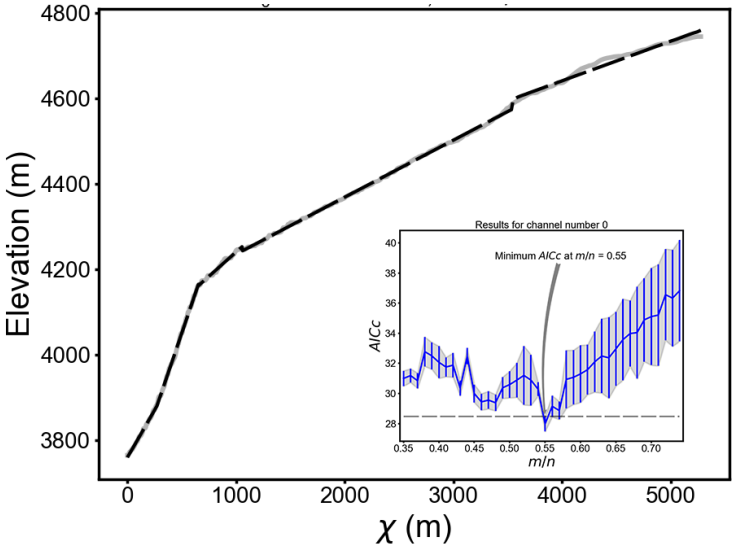

Figure S3. Chi plot analysis for the 30 m SRTM-C using *AICc* minimization (Mudd et al., 2014) implemented in Python (LSDTopoTools). Note the excellent fit (dashed black lines) achieved by breaking the channel (gray line) into segments. Resulting *m/n* = 0.55 at minimum *AICc*, with plausible values of 0.56 and 0.57.

S4. Results

S4.1. Elevation Accuracy

The following are additional vertical uncertainty plots with respect to elevation, slope, and aspect measured from each DEM.

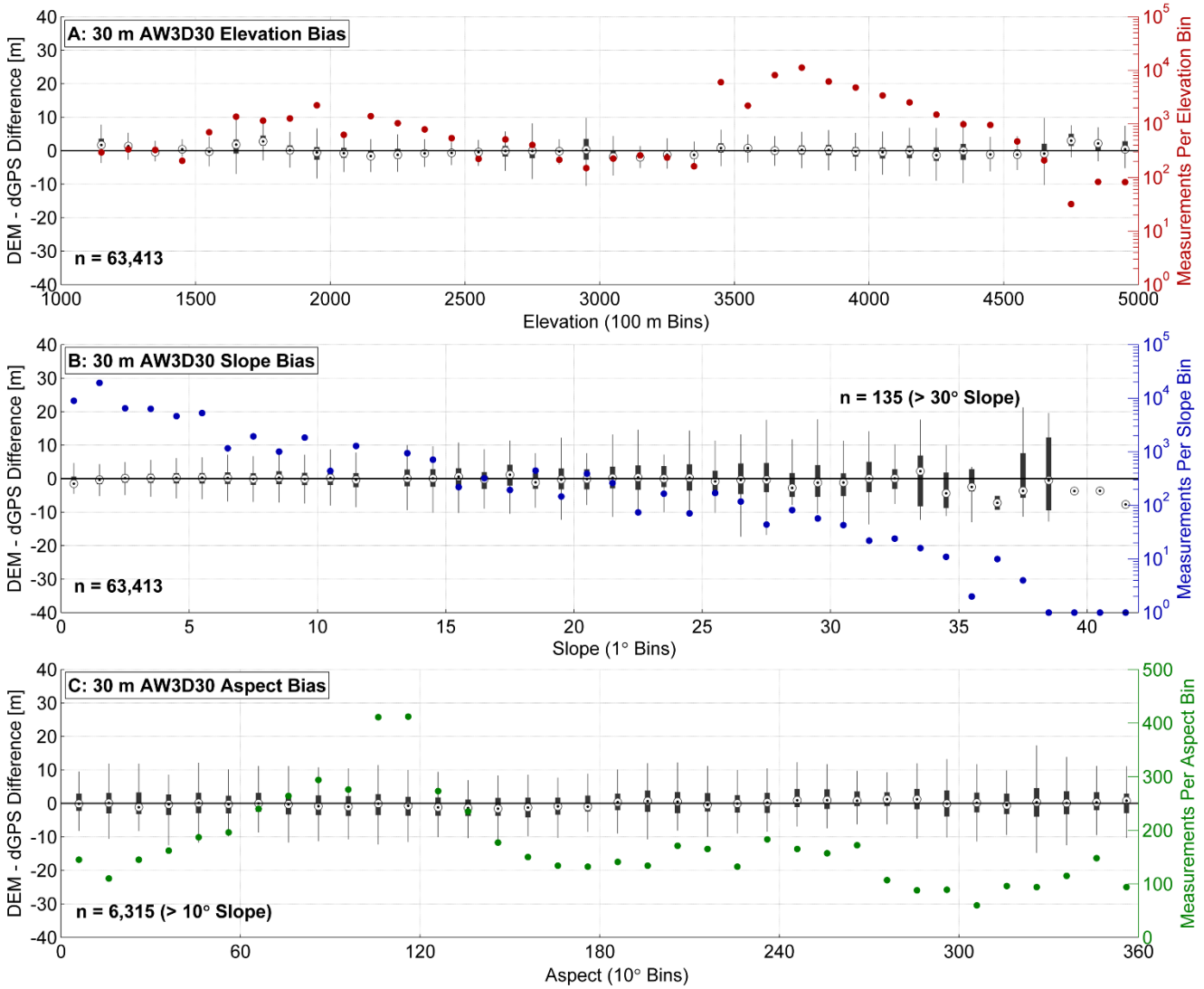

Figure S4. 30 m AW3D30 (A) elevation, (B) slope (eight-connected neighborhood calculated), and (C) aspect (eight-connected neighborhood calculated) vertical uncertainties. Median elevation difference (black unfilled circles) with 25-75th percentile range (boxes) and 1st and 99th percentile outlier cutoff (whiskers) plotted for each bin on left axis. Number of measurements indicated (n) with measurements per bin plotted as colored circles on right axis. For aspect (C), only measurements on slopes > 10° are used. Elevation differences are normalized by mean offset. We note the dearth of slope measurements > 30° (B).

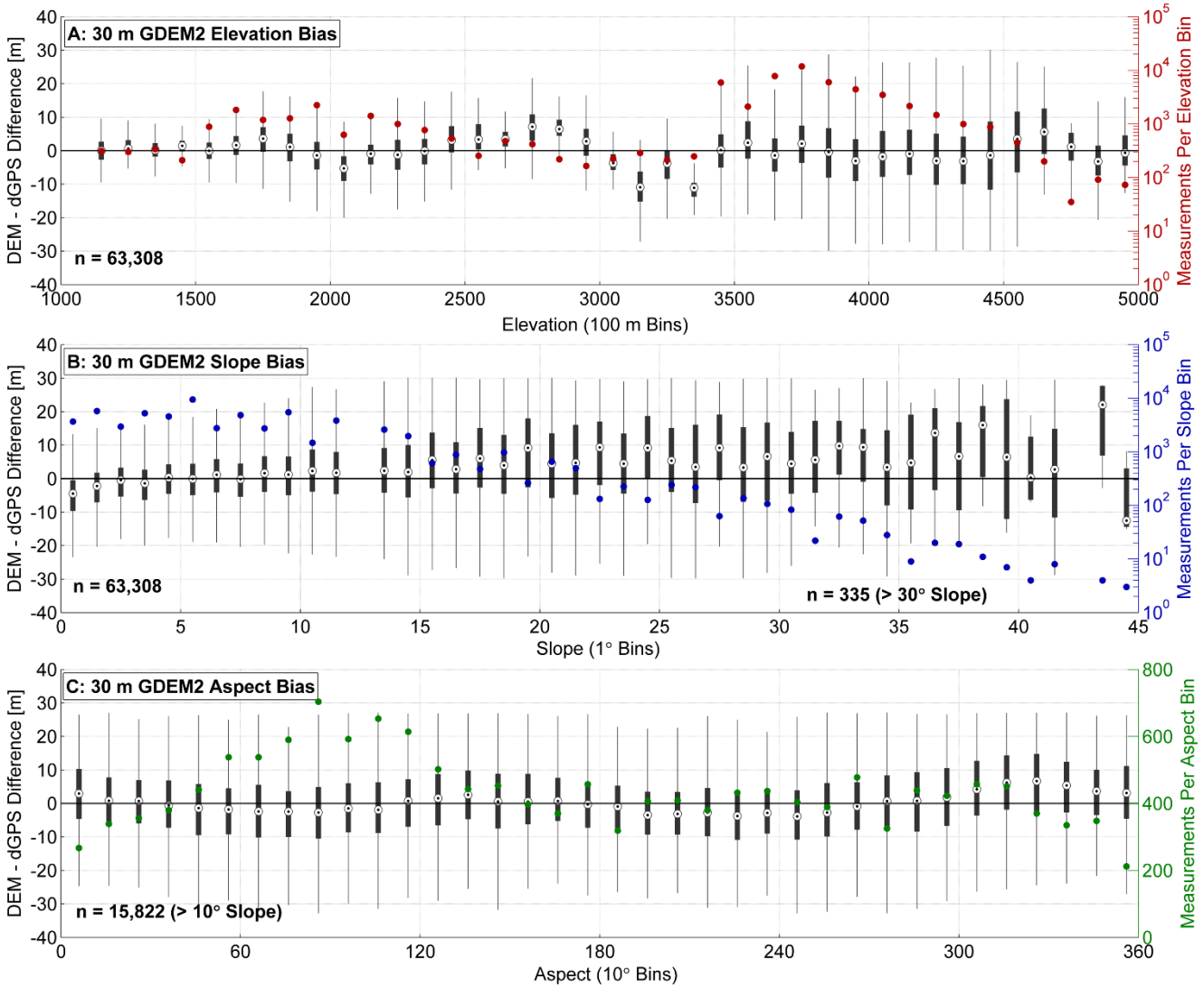

Figure S5. 30 m ASTER GDEM2 (A) elevation, (B) slope, and (C) aspect vertical uncertainty bias. Note the wide uncertainty range (bars and whiskers), large number of measurements taken from slopes > 10°, and ±5 m aspect bias for this noisy optically generated dataset.

5

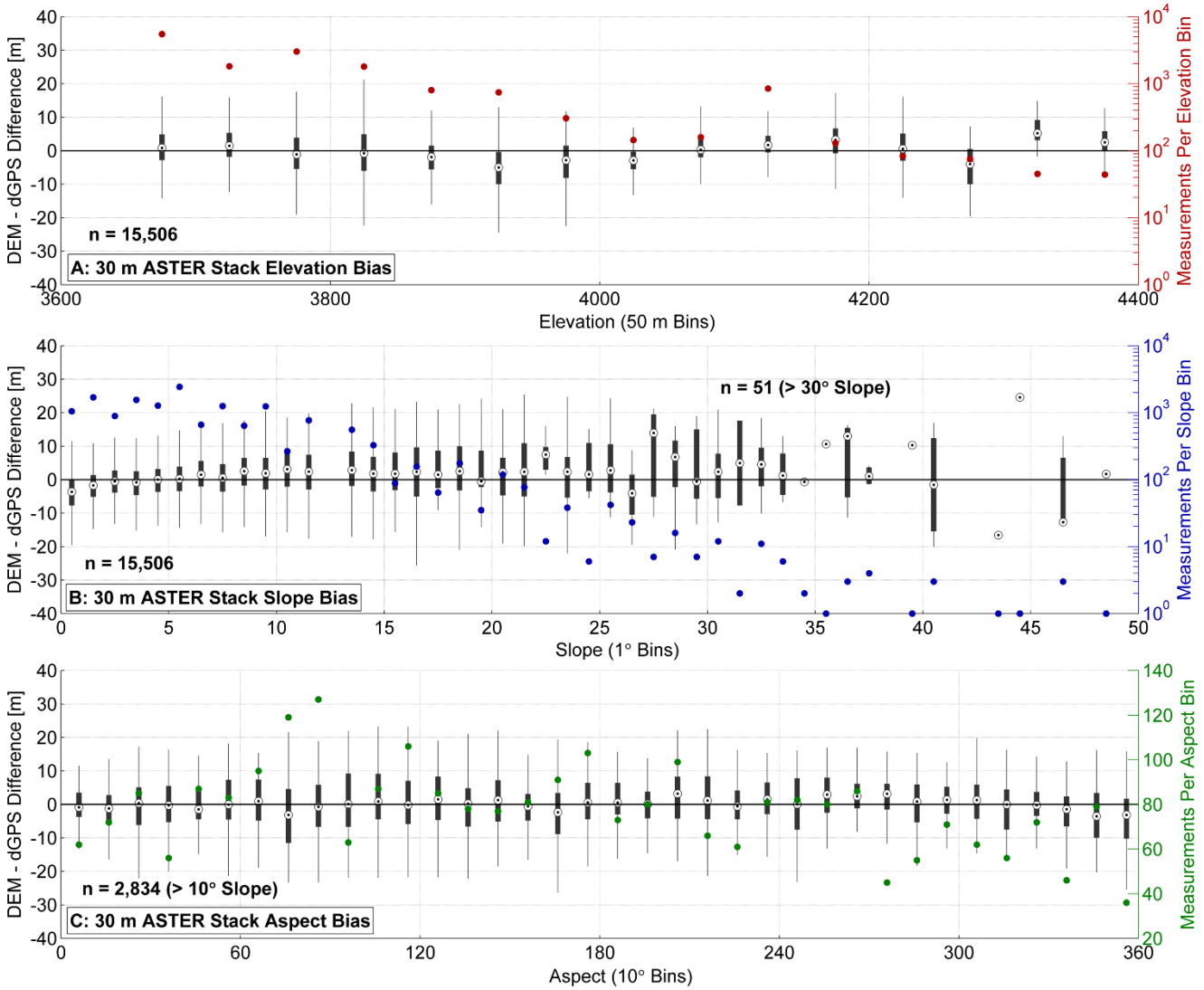

Figure S6. 30 m ASTER Stack (A) elevation, (B) slope, and (C) aspect vertical uncertainty bias. Note the wide uncertainty range similar to the ASTER GDEM2, but no clear aspect bias. This DEM covers only the Pocitos Basin (Fig. 1B), and thus a smaller elevation range than the GDEM2.

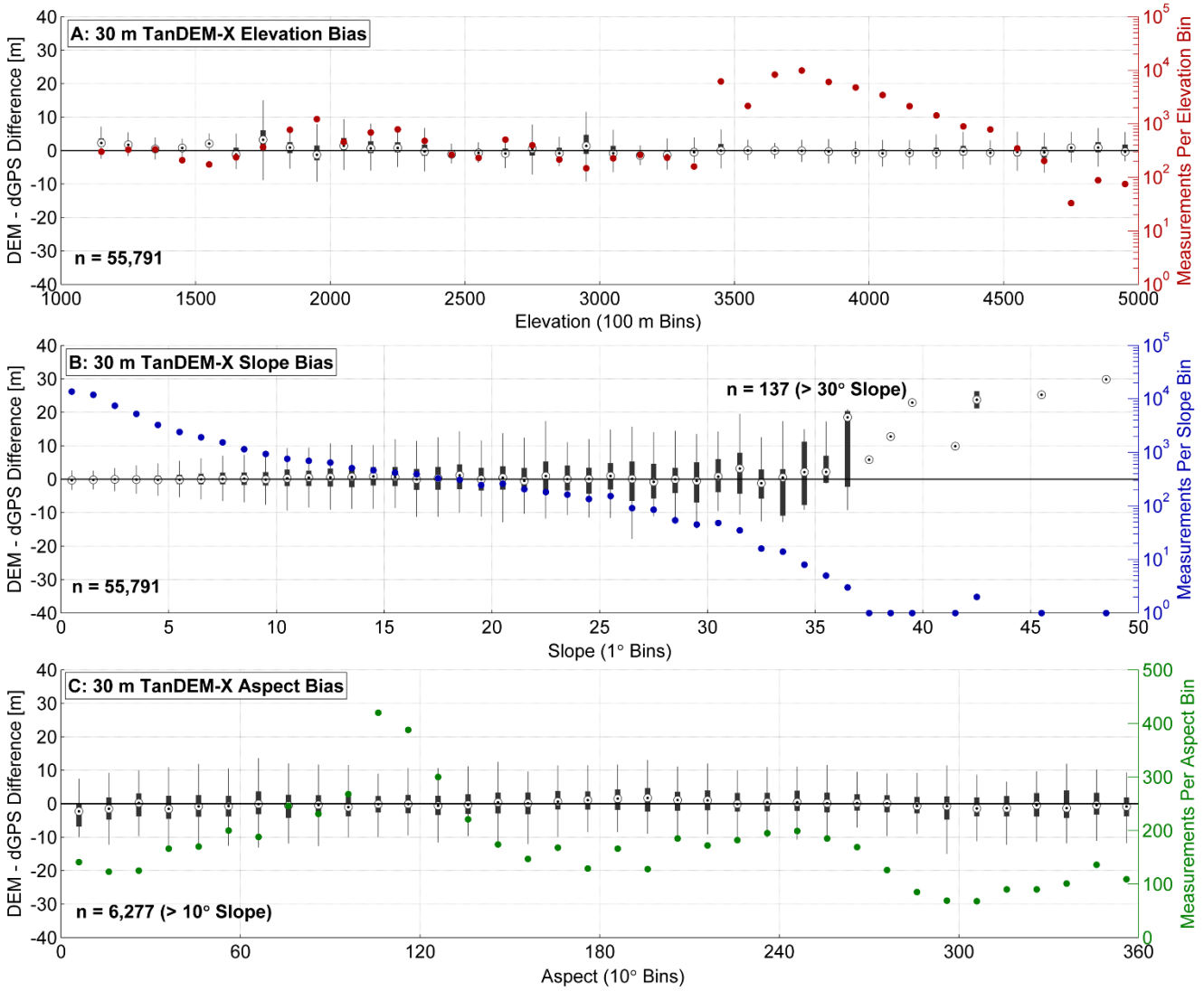

Figure S7. 30 m TanDEM-X (A) elevation, (B) slope, and (C) aspect vertical uncertainty bias. Trends are similar to the 12 m TanDEM-X (Fig. 6), however, error bars are larger in the 30 m version.

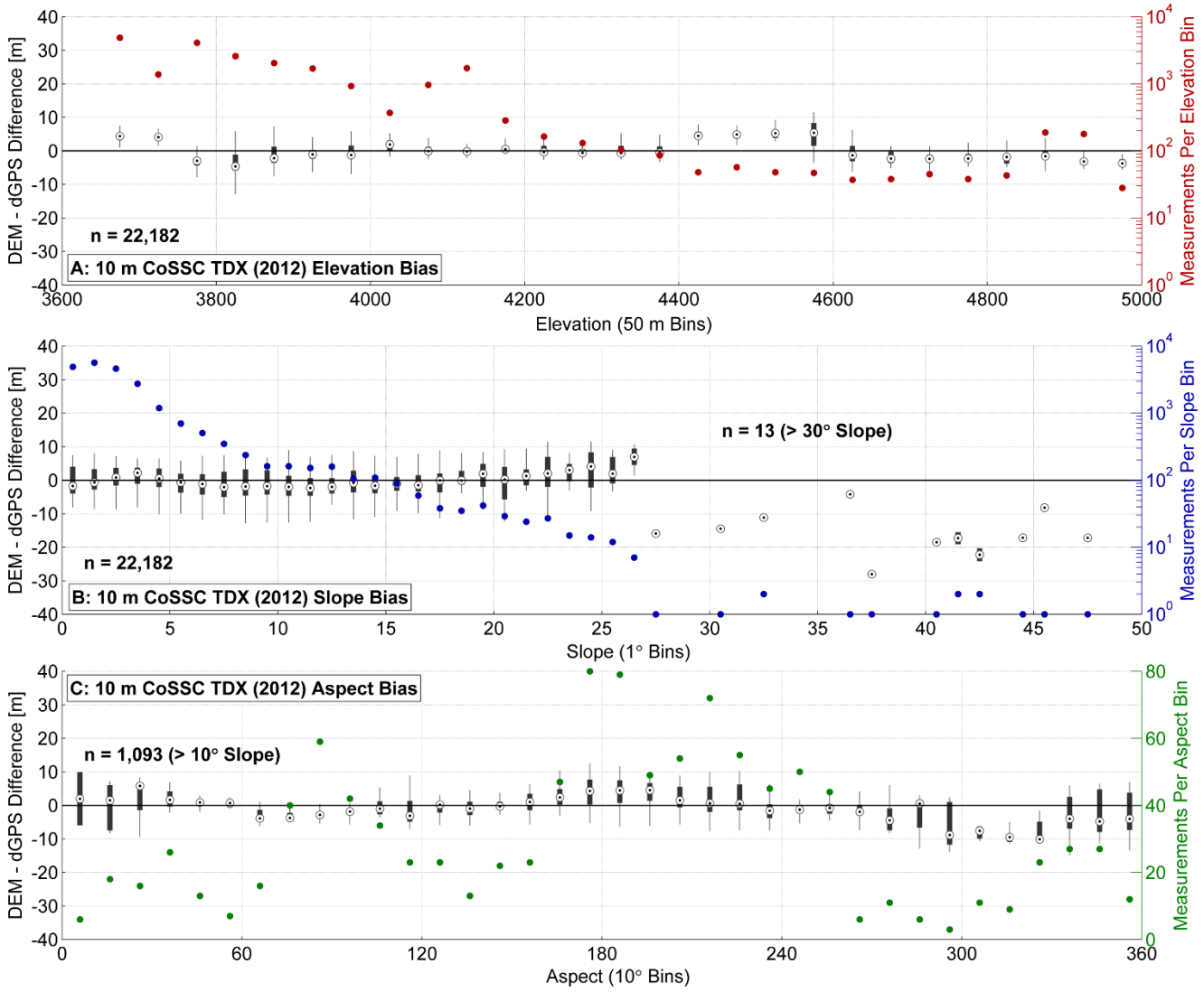

Figure S8. 10 m CoSSC TDX (6 November 2012) (A) elevation, (B) slope, and (C) aspect vertical uncertainty bias. Note the minor aspect bias, removed in the stacked TanDEM-X DEMs (Fig. 6).

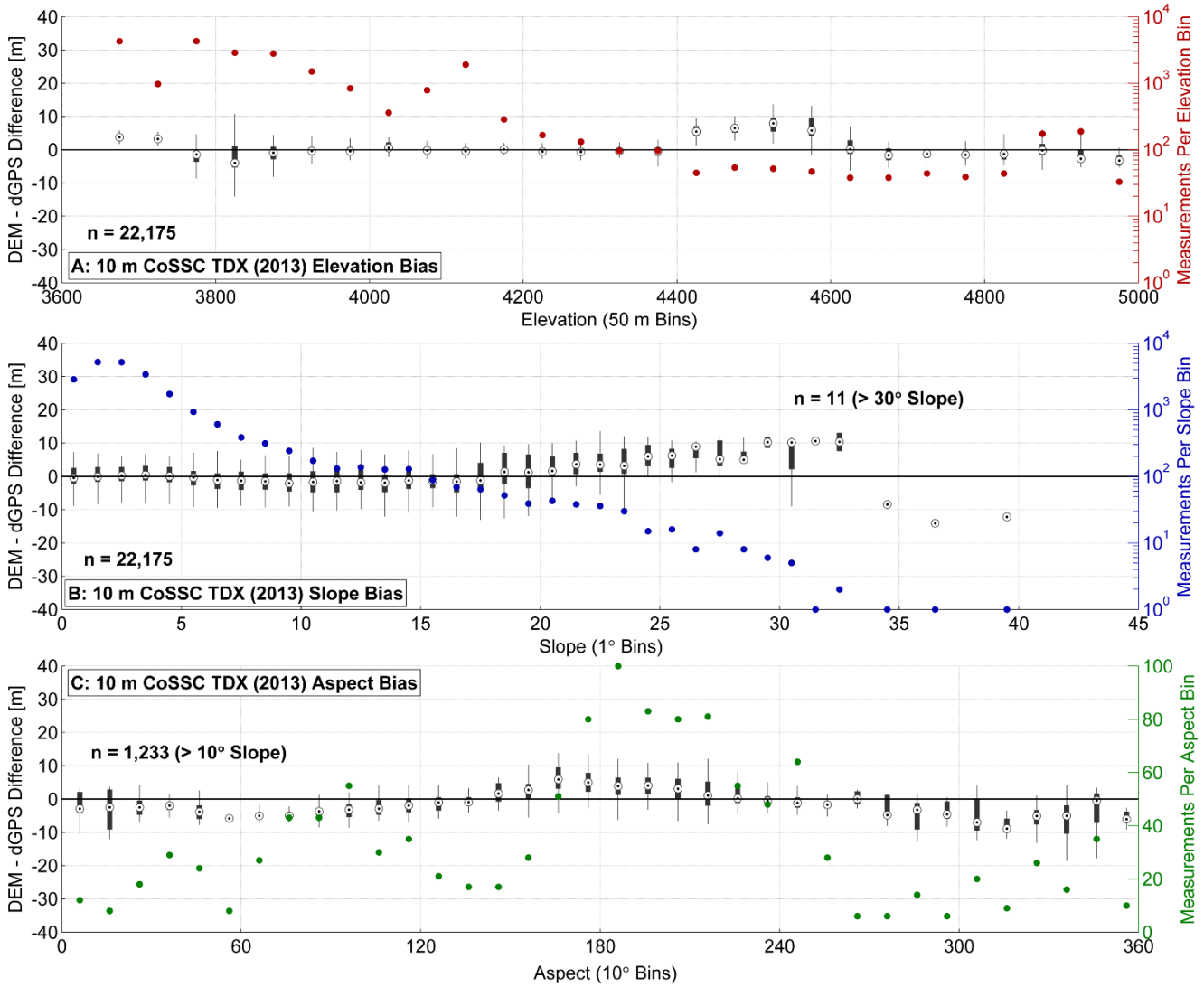

Figure S9. 10 m CoSSC TDX (25 August 2013) (A) elevation, (B) slope, and (C) aspect vertical uncertainty bias. Note the minor aspect bias, removed in the stacked TanDEM-X DEM (Fig. 6).

S4.3. 2D Fourier Analysis

In Fig. S10 we display the non-normalized 1D power spectra calculated from Eqs. (3) and (4) for the 30 m SRTM-C, 12 m TanDEM-X, and 5 m AW3D5 DEM clips. Plotted for each is the individual DFT elements and the linear regression through mean amplitude in 20 logarithmically spaced wavelength bins, which is used as the background spectrum to normalize the mean-squared amplitude in Fig. 12. A linear regression through logarithmically spaced wavelength bins (at the mean value) is used as the background spectrum to normalize the mean-squared amplitude, as opposed to the randomly generated surfaces in

Perron et al. (2008). Use of the median of the wavelength bins in the linear regression provided comparable results to the mean, with the R^2 value in all cases > 0.98. Although this linear regression is somewhat skewed by the longest wavelength (lowest frequency) values (Fig. S10), we are interested only in the high-frequency noise, which is effectively normalized here. Also noted in Fig. S10 is the regression slope of each line. Further details on the generation of these plots can also be found in Perron et al. (2008) and online at http://web.mit.edu/perron/www/downloads.html.

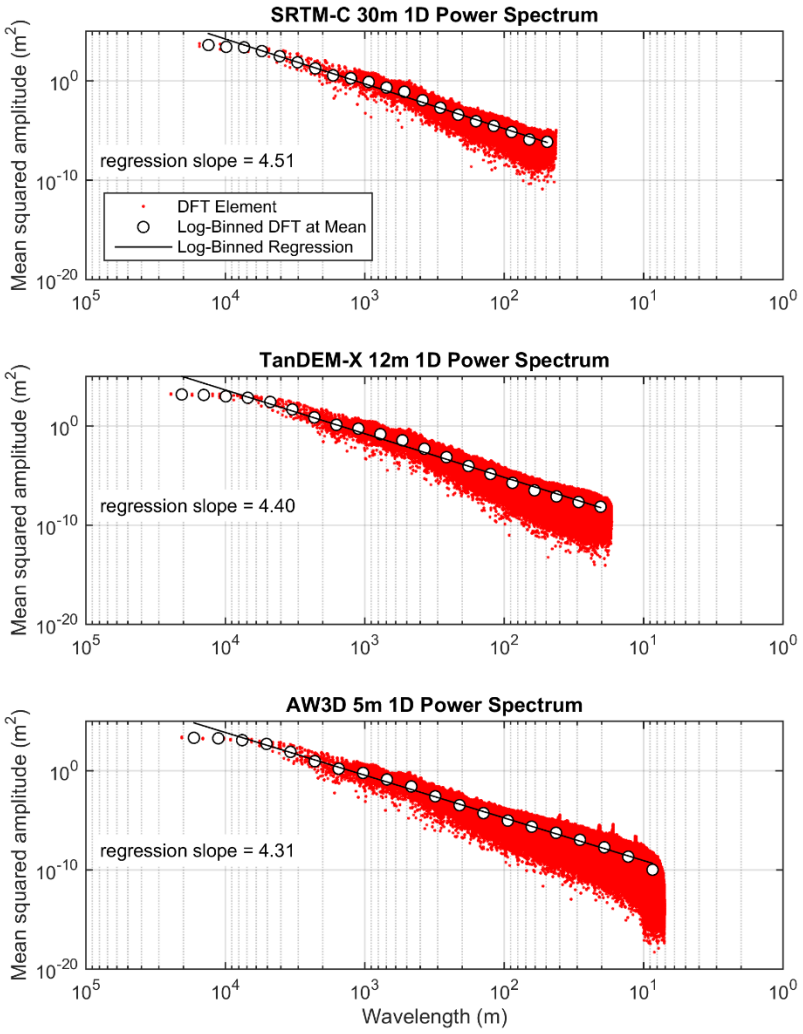

Figure S10. Non-normalized 1D power spectra for the three DEMs chosen for spectral analysis. The DFT elements and regression through 20 log-bins is depicted on each plot, with the slope of the regression line noted. Note the linear fit method does not fit to the highest wavelength (lowest frequency) domain, however, we are only interested in the high-frequency (low wavelength) signal here, which is normalized using the linear fit.

S5. Discussion

S5.2.2. Hillslopes

In Fig. S11, we demonstrate the effect of bilinear resampling the 5 m AW3D5 DEM to 10 m and 30 m. We compare the slope and curvature distributions of this resampled data with the 12 m TanDEM-X and 30 m SRTM-C, with the goal of demonstrating how changing the length scale of slope and curvature measurements is affected by DEM resolution (5-30 m) versus DEM type (radar for SRTM-C and TanDEM-X versus optical for AW3D5). In Fig. S11A greater magnitude slopes in the interquartile range are still measured in the AW3D5, even after resampling, when compared to the other datasets at their respective original resolutions. Slope outliers, however, remain similar. In Fig. S11B particularly, we note that there are a greater number of outlier measurements and wider interquartile range for the AW3D5 resampled. We note that this difference becomes reduced in the 30 m resampled AW3D5 and 30 m SRTM-C, whereas the difference is more apparent in the 10 m resampled AW3D5 compared to the 12 m TanDEM-X.

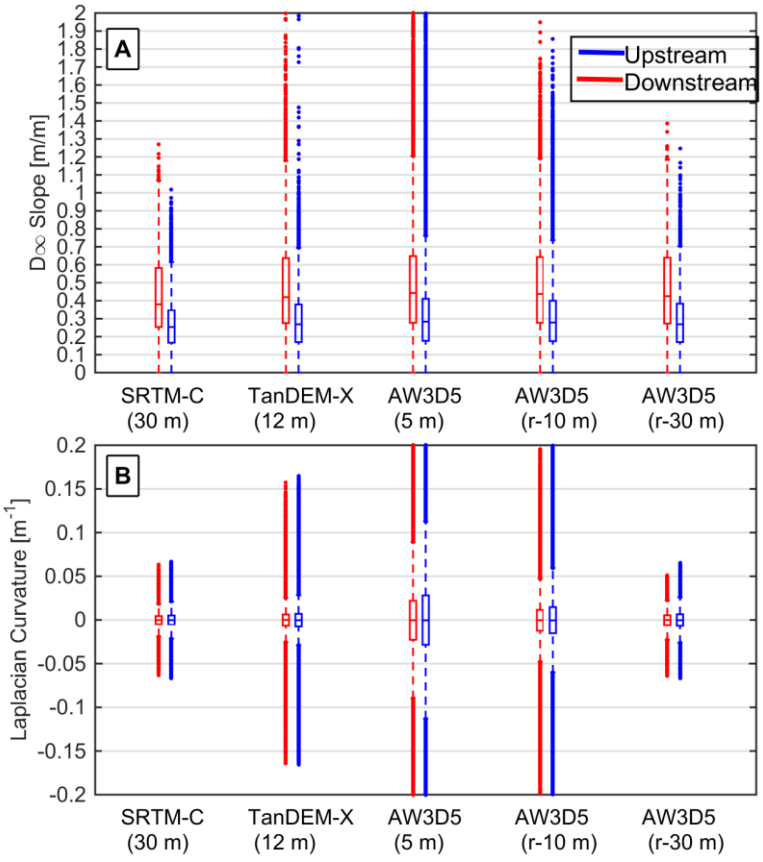

Figure S11. Slope (A) and curvature (B) box plots separated upstream (blue) and downstream (red) of the knickpoint. The AW3D5 DEM (native 5 m resolution) has been bilinear resampled (r) to 10 m and 30 m for comparison with TanDEM-X and SRTM-C. Slope and curvature are calculated in a 9 cell window. Center line is median, boxes are 25-75th percentile range, dashed whiskers extend to 1st and 99th percentiles, and all outliers are plotted as points. Note that in cases where the outliers extend out of range of the plots, the points are truncated.

References

Becek, K.: Investigation of elevation bias of the SRTM C-and X-band digital elevation models, International Archives of the Photogrammetry, Remote Sensing and Spatial Information Sciences, 37, 105-110, 2008.

Berthier, E., and Toutin, T.: SPOT5-HRS digital elevation models and the monitoring of glacier elevation changes in North-West Canada and South-East Alaska, Remote Sensing of Environment, 112, 2443-2454, 2008.

Berthier, E., Arnaud, Y., Vincent, C., and Rémy, F.: Biases of SRTM in high-mountain areas: Implications for the monitoring of glacier volume changes, Geophysical Research Letters, 33, 2006.

Farr, T. G., Rosen, P. A., Caro, E., Crippen, R., Duren, R., Hensley, S., Kobrick, M., Paller, M., Rodriguez, E., Roth, L., Seal, D., Shaffer, S., Shimada, J., Umland, J., Werner, M., Oskin, M., Burbank, D., and Alsdorf, D.: The Shuttle Radar Topography Mission, Reviews of Geophysics, 45, 2007.

Flint, J. J.: Stream gradient as a function of order, magnitude, and discharge, Water Resources Research, 10, 969-973, 1974.

Forte, A. M., Whipple, K. X., Bookhagen, B., and Rossi, M. W.: Decoupling of modern shortening rates, climate, and topography in the Caucasus, Earth and Planetary Science Letters, 449, 282-294, 2016.

Gonçalves, J. A.: Orientation and Dem Extraction From ALOS-PRISM Images Using The SRTM-DEM As Ground Control, Proceedings of the International Archives of Photogrammetry, Remote Sensing and Spatial Information Sciences, 1177-1182, 2008.

Gorokhovich, Y., and Voustianiouk, A.: Accuracy assessment of the processed SRTM-based elevation data by CGIAR using field data from USA and Thailand and its relation to the terrain characteristics, Remote Sensing of Environment, 104, 409-415, 2006.

Hack, J. T.: Studies of longitudinal stream profiles in Virginia and Maryland, 1957.

Hirano, A., Welch, R., and Lang, H.: Mapping from ASTER stereo image data: DEM validation and accuracy assessment, ISPRS Journal of Photogrammetry and Remote Sensing, 57, 356-370, 2003.

Jarvis, A., Reuter, H. I., Nelson, A., Guevara, E., and others: Hole-filled SRTM for the globe Version 4, available from the CGIAR-CSI SRTM 90m Database (http://srtm. csi. cgiar. org), 2008.

Kääb, A.: Combination of SRTM3 and repeat ASTER data for deriving alpine glacier flow velocities in the Bhutan Himalaya, Remote Sensing of Environment, 94, 463-474, 2005.

Kolecka, N., and Kozak, J.: Assessment of the Accuracy of SRTM C- and X-Band High Mountain Elevation Data: a Case Study of the Polish Tatra Mountains, Pure and Applied Geophysics, 171, 897-912, 2014.

Ludwig, R., and Schneider, P.: Validation of digital elevation models from SRTM X-SAR for applications in hydrologic modeling, ISPRS Journal of Photogrammetry and Remote Sensing, 60, 339-358, 2006.

Marschalk, U., Roth, A., Eineder, M., and Suchandt, S.: Comparison of DEMs derived from SRTM / X-and C-band, IEEE International IEEE International IEEE International Geoscience and Remote Sensing Symposium, 2004. IGARSS textquotesingle04. Proceedings. 2004, 4531-4534,

Mudd, S. M., Attal, M., Milodowski, D. T., Grieve, S. W. D., and Valters, D. A.: A statistical framework to quantify spatial variation in channel gradients using the integral method of channel profile analysis, Journal of Geophysical Research: Earth Surface, 119, 138-152, 2014.

Perron, J. T., Kirchner, J. W., and Dietrich, W. E.: Spectral signatures of characteristic spatial scales and nonfractal structure in landscapes, Journal of Geophysical Research, 113, 2008.

Perron, J. T., and Royden, L.: An integral approach to bedrock river profile analysis, Earth Surface Processes and Landforms, 38, 570-576, 2013.

Rexer, M., and Hirt, C.: Comparison of free high resolution digital elevation data sets (ASTER GDEM2, SRTM v2.1/v4.1) and validation against accurate heights from the Australian National Gravity Database, Australian Journal of Earth Sciences, 61, 213-226, 2014.

Rodriguez, E., Morris, C. S., and Belz, J. E.: A Global Assessment of the SRTM Performance, Photogrammetric Engineering & Remote Sensing, 72, 249-260, 2006.

Schwanghart, W., and Scherler, D.: Short Communication: TopoToolbox 2 textendash MATLAB-based software for topographic analysis and modeling in Earth surface sciences, Earth Surface Dynamics, 2, 1-7, 2014.

Shortridge, A., and Messina, J.: Spatial structure and landscape associations of SRTM error, Remote Sensing of Environment, 115, 1576-1587, 2011.

Smith, B., and Sandwell, D.: Accuracy and resolution of shuttle radar topography mission data, Geophysical Research Letters, 30, 2003.

Sun, G., Ranson, K. J., Kharuk, V. I., and Kovacs, K.: Validation of surface height from shuttle radar topography mission using shuttle laser altimeter, Remote Sensing of Environment, 88, 401-411, 2003.

Tachikawa, T., Kaku, M., Iwasaki, A., Gesch, D. B., Oimoen, M. J., Zhang, Z., Danielson, J. J., Krieger, T., Curtis, B., Haase, J., and others: ASTER global digital elevation model version 2-summary of validation results, 2011.

Tadono, T., Ishida, H., Oda, F., Naito, S., Minakawa, K., and Iwamoto, H.: Precise Global DEM Generation by ALOS PRISM, ISPRS Annals of Photogrammetry, Remote Sensing and Spatial Information Sciences, II-4, 71-76, 2014.

Takaku, J., Tadono, T., and Tsutsui, K.: Generation of High Resolution Global DSM from ALOS PRISM, The International Archives of Photogrammetry, Remote Sensing and Spatial Information Sciences, 40, 243-243, 2014.

Toutin, T., and Cheng, P.: DEM generation with ASTER stereo data, Earth Observation Magazine, 10, 10-13, 2001.

Trisakti, B., and Julzarika, A.: DEM generation from stereo ALOS PRISM and its quality improvement, International Journal of Remote Sensing and Earth Sciences (IJReSES), 2011.

Wessel, B.: TanDEM-X Ground Segment--DEM Products Specification Document, 2016.

Wiener, N.: Extrapolation, interpolation, and smoothing of stationary time series, MIT press Cambridge, 1949.

Wobus, C., Whipple, K. X., Kirby, E., Snyder, N., Johnson, J., Spyropolou, K., Crosby, B., and Sheehan, D.: Tectonics from topography: Procedures, promise, and pitfalls, in: Special Paper 398: Tectonics, Climate, and Landscape Evolution, Geological Society of America, 55-74, 2006.